Multistate Magnetization Switching Driven by Spin Current From a Ferromagnetic Layer

Yumeng Yang,[1,2] Hang Xie,[1] Yanjun Xu,[1] Ziyan Luo,[1] and Yihong Wu[1,*]

[1] *Department of Electrical and Computer Engineering, National University of Singapore, 4 Engineering Drive 3, Singapore 117583, Singapore*

[2] *School of Information Science and Technology, ShanghaiTech University, Shanghai 201210, China*

(Received 4 November 2019; revised manuscript received 27 January 2020; accepted 28 February 2020; published 30 March 2020)

Spin-charge interconversion in ferromagnets has recently drawn great attention due to its ability to generate spin current via the anomalous Hall, planar Hall, or intrinsic spin Hall effect. In this work, we demonstrate the magnetization switching of perpendicular anisotropy ferromagnets by the transversely polarized spin current generated from an easy-plane ferromagnet such as (Fe, Mn)Pt and (Co, Fe)B. The spin-torque efficiency is characterized to be about 21% of that of the same structure with the easy-plane ferromagnet replaced by Ta. In addition, we find that the magnetization switching consists of multiple intermediate states, which can be robustly set by the applied current pulse amplitude and repetition number. This behavior can be used to mimic synaptic devices that is potentially useful for neuromorphic computing.

DOI: 10.1103/PhysRevApplied.13.034072

I. INTRODUCTION

In the past decade, the spin-orbit torque (SOT) effect has been demonstrated as a promising technique to manipulate the magnetization of ferromagnets (FMs) [1–5]. Conventionally, SOT has been provided by either the spin current generated via spin Hall effect (SHE) in heavy metals (HMs) with strong spin-orbit coupling (SOC) or the spin accumulation from Rashba-Edelstein effect (REE) at the interface with structural inversion asymmetry. Recently, spin-charge interconversion in metallic FMs has attracted attention due to its ability in generating spin accumulation through anomalous Hall effect (AHE) or planar Hall effect (PHE) without the requirement of a HM [6–8]. In the case of AHE, with an electric field applied along x axis, the spin-polarized current flows along the z axis if the magnetization is along the y axis; while in the PHE scenario, when the magnetization has an inclining angle from the electric field, the spin-polarized current flows along the magnetization direction. In both cases, the spin polarization of spin current is aligned with the direction of magnetization (longitudinally polarized spin current), and therefore it offers an additional degree of freedom to control the direction of SOT induced by FMs by simply rotating its magnetization. Several experimental attempts have been made to demonstrate the AHE-related spin-charge interconversion in FMs. Notably, spin-pumping [9–11] or nonlocal spin-injection experiments [12–15] using FMs as both injector and detector have been realized in heterostructures consisting of $Y_3Fe_5O_{12}$/FM. The resulting SOT is further characterized to be comparable to that of HM in FM-normal metal (NM)-FM trilayers [16–18]. We discover an anomalous Hall magnetoresistance (AHMR) in Fe-based FM alloys [19], which correlates with the simultaneous action of AHE and its inverse effect in the FMs.

However, there are also recent experimental evidences suggesting that the interconversion process in FMs is more complicated than simply being driven by the AHE or PHE. In particular, spin current or spin accumulation with polarization transverse to the magnetization (transversely polarized spin current) has been observed near the FM-NM interface [20–22] or at the surfaces of FM single layers [23]. The former is attributed to interface-generated spin current with spin-polarization rotation through combined actions of spin-orbit filtering, precession, and scattering [24], while the latter is suggested by *ab initio* calculation to arise from an intrinsic origin that is universal to FMs in the clean limit [25,26]. Spin-swapping effect by impurity scattering inside FMs [27] is also theoretically proposed to be a source of the transversely polarized spin current. Although it still remains unclear whether the interface-generated spin current, spin swapping inside FMs, or intrinsic contribution governs the spin-charge interconversion process, magnetization switching [20,28–30] and self-oscillation [31,32] driven by spin current generated in FMs are experimentally demonstrated.

Very recently, we observe a sizable dampinglike SOT induced by surface spin rotation in symmetric

*elewuyh@nus.edu.sg

$MgO/Fe_{0.8}Mn_{0.2}/MgO$ structures [33], which acts on the magnetization in equivalence to a fieldlike effective field along the y direction in HM-FM bilayers. The experimental observations are successfully accounted for by the combined effect of AHE and spin rotation near the surfaces of a single FM layer. When an electric current flows in the x direction of a thin FM layer, both charge and spin accumulations occur at the sample surfaces due to AHE. In the interior of the FM layer, the spin poalrization of the sacttered electrons is aligned along the magnetization direction due to strong exchnage coupling. However, in the vicinity of the surface, the spin polarization of scattered electrons, in general, can be expressed a $\hat{\sigma}' = S\hat{n} + T\hat{n} \times (\hat{\sigma} \times \hat{n}) + U(\hat{n} \times \hat{\sigma})$, where S, T, and U are constants determined by the scattering angle and strength of SOC, $\hat{\sigma}$ is the initial polarization direction before scattering, and $\hat{n}$ is the unit vector parallel to the y axis (in plane and transverse to the current) [24,34–36]. The accumulated spins diffuse back from the surface and thereby extert a torque on the magnetization of the FM. Similar to the transfer of spin angular momentum from a nonlocal source to a local magnetic moment ($\hat{m}$) in HM-FM heterostructures, the spin torque here has the form of $\hat{\tau}_{ST} = \hat{m} \times (\hat{m} \times \hat{\sigma}')$ [37–40]. The resulting torque can be written as $\hat{\tau}_{ST} = [S - \text{sign}(\sigma)T\hat{m} \cdot \hat{n}]\hat{m} \times (\hat{m} \times \hat{n}) + \text{sign}(\sigma)U\hat{m} \times \hat{n}$, where $\hat{\sigma} = \text{sign}(\sigma)\hat{m}$, and $\text{sign}(\sigma) = 1$ (-1) for down (up) spins. As both $\hat{\sigma}$ and $\hat{n}$ change sign between top and bottom surfaces, the second term simply adds up at the two surfaces for up- and down-spin electrons and the combined effect is equivalent to a fieldlike torque in HM-FM bilayers as demonstrated in our previous work [33]. However, the first term is partially canceled out from the contributions of the top and bottom surfaces due to the opposite sign of spin-up and spin-down electrons, and therefore makes it difficult to detect it in a single-layer structure. In order to verify the presence of the first term by suppressing the cancelation from the bottom surface, in this work, we form a FM1-Ti-FM2 trilayer structure, in which FM1 is an easy-plane ferromagnet, whereas FM2 exhibits a perpendicular magnetic anisotropy (PMA). In this case, FM1 functions as an AHE-based spin source and FM2 as a spin detector. Instead of diffusing backward, the spin accumulation at the top surface of the FM1 layer can also travel across the Ti spacer and exert torque on the magnetization of the FM2 layer. In this case, since the first term of $\hat{\tau}_{ST}$ is an in-plane dampinglike torque, it is expected that it leads to magnetization switching of FM2 under an assistive field in x direction, similar to the case in conventional HM-FM bilayers.

As revealed in our previous studies, the Fe-based alloys with large SOC tend to have large spin-charge interconversion efficiencies. Therefore, in this study, $(Fe_{0.71}Mn_{0.29})_{0.6}Pt_{0.4}$ or $Co_{20}Fe_{60}B_{20}$ with in-plane magnetic anisotropy (IMA) is chosen to generate the spin current (FM1), and a top (Co, Fe)B layer with PMA is chosen as the spin detector (FM2). Between the two FM layers, a Ti spacer is inserted to both decouple the two FMs and enhance the PMA of FM2. It should be noted that the IMA of FM1 and PMA of FM2 is confirmed with superconducting quantum interference device (SQUID) magnetometer measurements on coupon films. Current induced magnetization switching of the top PMA-(Co, Fe)B is realized in both structures using either the IMA-(Fe, Mn)Pt or IMA-(Co, Fe)B as the spin-current generator, with switching percentages of 56 and 78%, respectively. The spin-torque efficiency, which is characterized using the current-induced hysteresis loop-shift method, turns out to be around 21% of that of the same structure but with FM1 being replaced by Ta. Finally, we find that the magnetization switching has multiple intermediate states. By tuning the amplitude or repetition number of the applied current pulse, different intermediate states can be set and maintained. This behavior mimics the long-term potentiation and depression effect of a synaptic device that can be potentially useful for the supervised training process in neuromorphic computing systems.

II. EXPERIMENTAL METHODS

Samples with the structures of (starting from substrate side) FM1(5 or 9)/Ti(1–3)/(Co, Fe)B(1.2)/MgO(2)/Ta(2), as illustrated in Fig. 1(a), are deposited on SiO_2(300 nm)/Si substrates. Here, FM1 denotes either (Co, Fe)B(5) or (Fe, Mn)Pt(9). The numbers inside the parentheses indicate the thickness in nanometers. The Ta capping layer is used to prevent the degradation of MgO in ambient. Except for the Ti layer, which is prepared in an evaporation chamber, all other layers are deposited in a magnetron sputtering chamber. The (Fe, Mn)Pt layers are prepared by co-sputtering the $Fe_{0.8}Mn_{0.2}$ and Pt targets. All the layers are deposited in a multichamber system at a base pressure below 3×10^{-8} Torr and a working pressure of 3×10^{-3} Torr (for sputtering) without breaking the vacuum. To further promote the formation of PMA in the top (Co, Fe)B layer, post annealing is carried out at 250 °C in a furnace under a vacuum of 1×10^{-5} Torr. Standard photolithography and dry-etching methods are used to fabricate the Hall cross with a dimension of 100×10 μm^2 as illustrated in Fig. 1(a). Hall measurements are performed for all the samples in a home-built magneto-transport system.

III. RESULTS AND DISCUSSION

A. Hall measurements driven by magnetic field

Figures 1(b) and 1(c) show the magnetic field dependence of the Hall resistance of the (Fe, Mn)Pt(5 or 9)/Ti(t_{Ti})/(Co, Fe)B(1.2)/MgO(2)/Ta(2) samples for applied field in z and x direction, respectively. To optimize the PMA of the (Co, Fe)B layer with a fixed thickness of

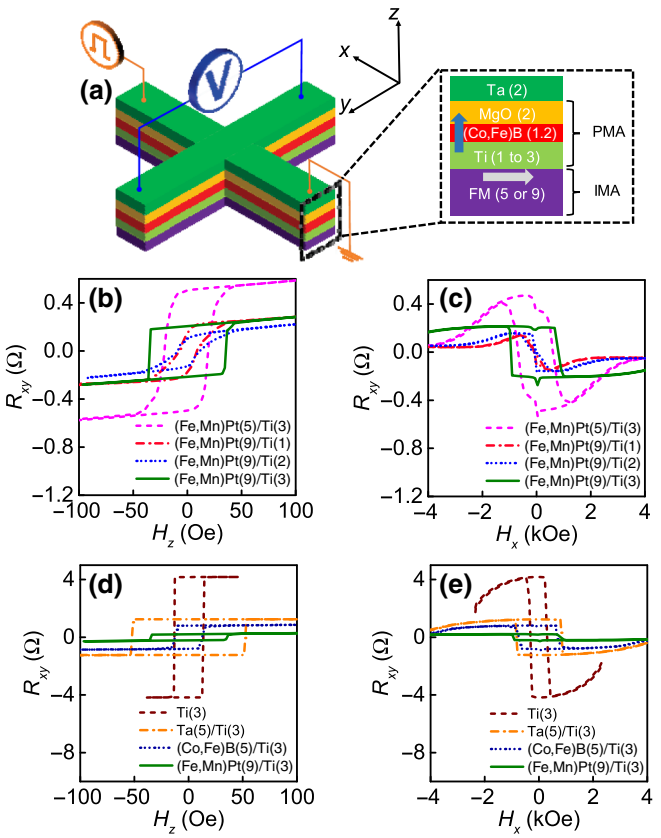

FIG. 1. (a) Left: schematic illustration of the Hall cross device and measurement geometry. Right: structure of the trilayer samples consisting of FM1(IMA)/Ti(spacer)/(Co, Fe)B(PMA)/MgO/Ta(cap) with FM1 = (Co, Fe)B or (Fe, Mn)Pt. (b), (c) Hall resistance of the (Fe, Mn)Pt(5 or 9)/Ti(t_{Ti})/(Co, Fe)B/MgO/Ta samples with $t_{Ti} = 1$–3 nm for applied field in z and x direction, respectively. (d), (e) Comparison of the Hall resistance of the (Fe, Mn)Pt and (Co, Fe)B samples with Ti and Ta control samples with the applied field in z and x direction, respectively. Note that the structure (Co, Fe)B(1.2)/MgO(2)/Ta(2) are omitted in the legends in (b)–(e) for simplicity.

1.2 nm, the Ti layer thickness (t_{Ti}) is varied in the range of 1 to 3 nm, whereas the thickness of (Fe, Mn)Pt is set at either 5 or 9 nm. When a small field is swept in z direction, corresponding to the case of Fig. 1(b), the AHE signal mainly comes from the (Co, Fe)B layer and its magnitude is proportional to the normalized z component of magnetization (m_z), i.e., $R_{xy}(H) = R_{AHE}\cos\theta$, where θ is the angle between the magnetization and z direction, H is the external field, and R_{AHE} is the saturation AHE resistance. On the other hand, due to the large demagnetizing field, the z component of the (Fe, Mn)Pt magnetization is only slightly tilted in the small field range. Therefore, the intercept of AHE curve with the y axis at $H = 0$ Oe is the R_{AHE} of (Co, Fe)B. From the shape of the AHE curve, we can see clearly that only the (Co, Fe)B deposited on top of (Fe, Mn)Pt(9)/Ti(3) exhibits good PMA. The square-shaped AHE curve at this Ti thickness also suggests that the magnetostatic coupling between the two FMs is very weak. The coupling if any will tilt the PMA-(Co, Fe)B away from its easy axis and thus gives a slanted curve instead of a square one. The good PMA is also reflected in the AHE curve obtained by sweeping the field in x direction as shown in Fig. 1(c). Compared to other samples, it is more difficult to orient the magnetization of this sample in the plane as represented by the slow decline of R_{xy} in the large field range. It should be noted that the hysteresis in the curve is due to the small field misalignment towards the z direction [41]. Moreover, the small drop in the center of the curves is due to the PHE of (Fe, Mn)Pt since it is IMA and can be saturated easily with an in-plane field. Since the PHE resistance of PMA-(Co, Fe)B is always around 1 order of magnitude smaller than the AHE resistance [42,43], it is therefore also not discernable in Fig. 1(c). This is supported by the almost same magnitude of R_{xy} in both the x- and z-direction curves. In general, the increase of Ti thickness can promote PMA in the sense that it can inhibit atomic diffusion [44,45] and interface intermixing [46] or enable CoFe nucleation from the MgO interface [47]. But it is detrimental for the spin current generated by the bottom FM1 layer to travel across the Ti and reach the (Co, Fe)B layer. Therefore, in this work, we fixed the Ti thickness at 3 nm unless otherwise stated. Figures 1(d) and 1(e) further compare the Hall resistance of the (Fe, Mn)Pt(9)/Ti(3)/(Co, Fe)B(1.2)/MgO(2)/Ta(2) [hereafter we refer it to as the (Fe, Mn)Pt sample] and (Co, Fe)B(5)/Ti(3)/(Co, Fe)B(1.2)/MgO(2)/Ta(2) [hereafter we call it the (Co, Fe)B sample] with the control samples of Ti(3)/(Co, Fe)B(1.2)/MgO(2)/Ta(2) (Ti control sample) and Ta(5)/Ti(3)/(Co, Fe)B(1.2)/MgO(2)/Ta(2) (Ta control sample) with the applied field in z and x direction, respectively. It is apparent that all these samples exhibit well-defined PMA behavior. In addition, from the x-direction field sweeping curves in Fig. 1(e), the effective magnetic anisotropy field (H_k) can be estimated using a macrospin approximation as [41] $H_k = (H/\cos\theta)$. For simplicity, we ignore the small possible field misalignment since it is consistent among all samples, and therefore it does not affect the discussion afterwards. The estimated H_k value is thus 4.4, 4.4, 5.8 and 5.6 kOe for the Ta control, (Co, Fe)B, (Fe, Mn)Pt, and Ti control samples, respectively.

B. Magnetization switching measurements driven by pulsed current

Next we proceed to describe the current-induced magnetization-switching measurements for the PMA samples whose AHE curves are shown in Figs. 1(d) and 1(e). The typical measurement sequences are illustrated in Fig. 2(a). Current pulses with a constant duration

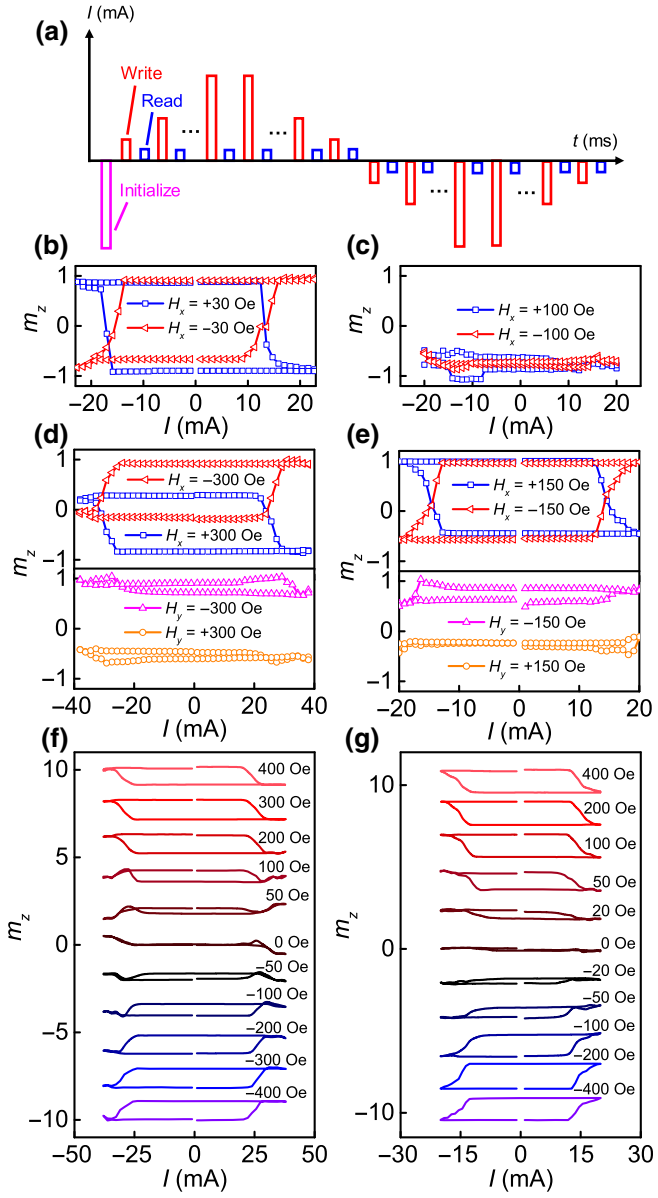

FIG. 2. (a) Measurement procedure of the magnetization switching driven by pulsed current. (b), (c) Results of Ta and Ti control samples with assistive field in x direction, respectively. (d), (e) Results of (Fe, Mn)Pt and (Co, Fe)B samples with the assistive field in x or y direction, respectively. (f), (g) Results of (Fe, Mn)Pt and (Co, Fe)B samples with varying x-direction assistive field in the range of ± 400 Oe, respectively. Note that the curves in (f) and (g) are vertically shifted for clarity. m_z is the normalized z component of magnetization.

of 2 ms and duty ratio of 1% but varying amplitude are applied in x direction. Similar switching behaviors can also be observed with pulse width down to 200 μs and duty ratio of 0.1% for the results presented hereafter, which suggests that the Joule heating effect and the associated device temperature rise is not significant. In between two adjacent writing pulses, the magnetization state of the top PMA-(Co, Fe)B is read by current pulses with the same duration and duty ratio as that of the writing pulse but at a much smaller amplitude of 1 mA. The measurement always began by using a large writing pulse to initialize the state, and then sweeping the current pulses in the opposite direction by gradually increasing its amplitude in a stepwise manner. Figures 2(b) and 2(c) show the results from the control samples of Ta and Ti, respectively. Instead of R_{xy}, we plot m_z as a function of the current pulse amplitude for a better representation of the magnetization direction of PMA-(Co, Fe)B. An x-direction assistive field is applied to achieve deterministic switching as in the case of conventional SOT. As can be seen, the SOT of the Ta control sample is able to drive an almost full magnetization switching (about 90%) at a current density of 1.36×10^7 A cm^{-2} [Fig. 2(b)]. Hereafter, for simplicity, we assume that all the current flows in the bottom HM or FM1 layer. In contrast, the current in the Ti layer has negligible effect on the magnetization of the neighboring (Co, Fe)B layer. Since the switching current density of the Ta/Ti/(Co, Fe)B/MgO/Ta sample is on the same order of those for Ta/(Co, Fe)B/MgO/Ta samples reported in the literature [48], it is safe to conclude that other than the charge-current shunting and small spin-current absorption, the influence or contribution of the Ti spacer to the spin torque can be neglected.

After having clarified the role of Ti, we now examine current-induced magnetization switching in the (Fe, Mn)Pt and (Co, Fe)B samples with the assistive field applied in either x or y direction, and the results are shown in Figs. 2(d) and 2(e), respectively. In both types of samples, the magnetization can only be deterministically switched in the presence of an assistive field in x direction, which resembles the behavior of the conventional HM-FM bilayer. Maximum switching percentages of 56 and 78% are realized in the (Fe, Mn)Pt and (Co, Fe)B samples at a critical current density (j_c) of 1.92×10^7 A cm^{-2} and 1.52×10^7 A cm^{-2}, respectively. Furthermore, we vary the strength of the assistive field in the range of ± 400 Oe. As seen in Figs. 2(f) and 2(g), the switching percentage diminishes with the decrease of the assistive field before it finally vanishes at zero field. We also perform the current-induced switching measurements without an assistive field after magnetizing the bottom (Fe, Mn)Pt or (Co, Fe)B layer along $\pm x$ or $\pm y$ direction. We do not observe any deterministic switching in all the cases (results are not shown here). The observations mentioned above suggest that the spin current generated in the bottom FM1 layer indeed can switch the top FM2 layer in the same fashion as the conventional HM. These results confirm the existence of the transversely polarized spin current near the interface of FM1, as reported previously [33], though further studies are required to provide direct evidences.

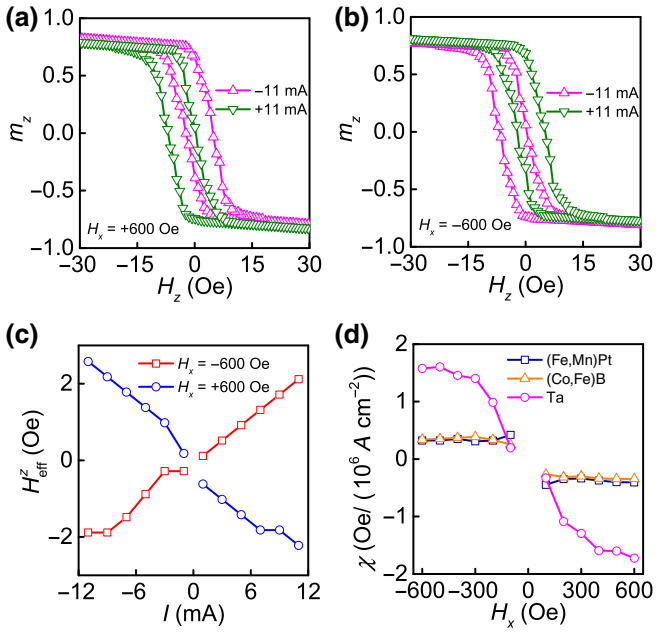

FIG. 3. (a), (b) The $m_z - H_z$ hysteresis loops for the (Fe, Mn)Pt sample with $H_x = +600$ Oe and –600 Oe at a bias current of ± 11 mA, respectively. (c) Hysteresis loop shift H_{eff}^z as a function of current under different applied currents at $H_x = \pm 600$ Oe, respectively. (d) Summary of the χ values for the Ta control, (Co, Fe)B and (Fe, Mn)Pt samples in the H_x range of ± 600 Oe.

C. Characterization of spin-torque efficiency

To have a more quantitative understanding, we characterize the effective field by using the current-induced hysteresis-loop-shift method [23,48,49]. With a bias field applied along x direction (H_x), the Néel-type domain walls in the top PMA layer experience a dampinglike SOT effective field in z direction. Therefore, when measuring the Hall resistance with sweeping field in z direction, the obtained hysteresis loop shifts along the sweeping-field direction, and the center of the shifted hysteresis loop (H_{eff}^z) corresponds to the SOT effective field. As an example, Figs. 3(a) and 3(b) show the m_z–H_z hysteresis loops for the (Fe, Mn)Pt sample with $H_x = +600$ and –600 Oe at a bias currents of ± 11 mA, respectively. As expected, there is a shift of the hysteresis loop with the shifting direction determined by both the applied current and H_x. This is consistent with the SOT-induced magnetization switching results in Fig. 2, and also resembles the behavior of SOT-induced magnetization switching in HM-FM bilayers.

Furthermore, we measure the hysteresis loops of the same sample under different applied currents at $H_x = \pm 600$ Oe, respectively, and plot H_{eff}^z as a function of current in Fig. 3(c). The linear relationship of H_{eff}^z against current clearly excludes Joule heating as the cause for the shift. By calculating $\chi = H_{\text{eff}}^z / j$ with j as the current density, the SOT efficiency (χ) can be obtained at the respective bias fields. Figure 3(d) summarizes the χ values for the Ta control, (Co, Fe)B and (Fe, Mn)Pt samples in the H_x range of ± 600 Oe. The data in the small field region between ± 100 Oe are not included since both the bottom IMA-(Co, Fe)B and IMA-(Fe, Mn)Pt are not well saturated in this region. As seen, the sign of SOT in both (Co, Fe)B and (Fe, Mn)Pt samples is the same as that of the SOT in the Ta sample. The H_x dependence of χ can be attributed to the domain expansion or shrinking of the PMA layer [48]. From the saturation value of χ (χ_{sat}) above ± 300 Oe, a spin Hall like angle (θ_s) can be estimated from the relation $\theta_s = (2/\pi)(2e\mu_0 M_s t \chi_{\text{sat}}/\hbar \cos\phi)$[48,50], with ϕ the angle between the domain-wall moment and the x axis, M_s the saturation magnetization, t the thickness of PMA-(Co, Fe)B, $\hbar$ the reduced Planck constant and e the electron charge. In the case of Neel-type domain walls, $\cos\phi = 1$ ($\cos\phi = -1$) for up-down (down-up) domain walls. By taking $M_s = 900$ emu cm^{-3}, $t = 1.2$ nm, and $\chi_{\text{sat}} = -1.60$ Oe/(10^6 A cm^{-2}), -0.34 Oe/(10^6 A cm^{-2}) and -0.35 Oe/(10^6 A cm^{-2}), θ_s can be obtained as -0.033, -0.007 and -0.007 for Ta, (Co, Fe)B and (Fe, Mn)Pt, respectively. Table I further summarizes the key parameters including effective anisotropy field, switching critical current density, switching percentage, and spin-torque efficiency for the different samples. It is noticed that χ_{sat} of Ta and (Co, Fe)B is much smaller than the reported values of Ta [-5.0 Oe/(10^6 A cm^{-2})] [48] and (Co, Fe)B [-0.60 Oe/(10^6 A cm^{-2})] [30] in similar structures using the same characterization method. The discrepancy may come from the fact that during the extraction of SOT efficiencies, no charge-current shunting nor spin-current absorption by the Ti layer is considered. Another possibility is that the SOT efficiencies are not a fundamental material parameter, but rather a device performance parameter. This means that even for the same material system, the different device preparation or treatment conditions may lead to the difference in efficiencies due to the variation of the interface qualities [51]. Nevertheless, it is safe to state that the SOT efficiency in (Co, Fe)B or (Fe, Mn)Pt is about 21% of the SOT efficiency in Ta. It is worth noting that the χ_{sat} values for (Co, Fe)B and (Fe, Mn)Pt are in the same range of the effective field efficiency in y direction we obtained previously for single-layer $Fe_{0.8}Mn_{0.2}$ layer, which is in the range of 0.2–0.4 Oe/(10^6 A cm^{-2}) [33].

D. Multistate magnetization switching behavior

Finally, we demonstrate the memristive behavior of the magnetization switching, which has potential applications as synaptic devices in neuromorphic computing. From Figs. 2(d) and 2(e), it is clear that the switching of m_z is not abrupt, but rather it has many intermediate states. By limiting the maximum writing current pulse magnitude in the range of 12–25 mA, a series of hysteretic loops

TABLE I. Summary of effective anisotropy field, switching critical current density, switching percentage, and SOT efficiency for the four types of the samples, respectively.

Sample type	H_k (kOe)	j_c (10^7 A cm^{-2})	Switching percentage (%)	χ_{sat} [Oe/(10^6 A cm^{-2})]	θ_s
Ta/Ti/(Co, Fe)B/MgO/Ta	4.4	1.36	90	−1.60	−0.033
(Co, Fe)B/Ti/(Co, Fe)B/MgO/Ta	4.4	1.52	78	−0.34	−0.007
(Fe, Mn)Pt/Ti/(Co, Fe)B/MgO/Ta	5.8	1.92	56	−0.35	−0.007
Ti/(Co, Fe)B/MgO/Ta	5.6	N. A.	N. A.	N. A.	N. A.

can be obtained as shown in Fig. 4(a) for the (Co, Fe)B sample at $H_x = -150$ Oe. This suggests that there are multiple intermediate states in the switching process and the final m_z state can be set into these states by changing the amplitude of the writing current. The results suggest that the switching process of the device starts with the nucleation of reversed domains with a size much smaller than the device size, and then followed by a thermally assisted domain-wall depinning process until it eventually leads to a complete switching by domain-wall propagation [52]. Since the energy barriers of the domain nucleation and the domain-wall depinning and propagation are dependent on the applied current amplitude [53,54], it naturally leads to a different percentage of magnetization reversal upon varying the current amplitude, which is reflected as many intermediate states. To confirm the effectiveness of this writing scenario, we perform repeated write-and-read measurements following the input current pulse sequence as

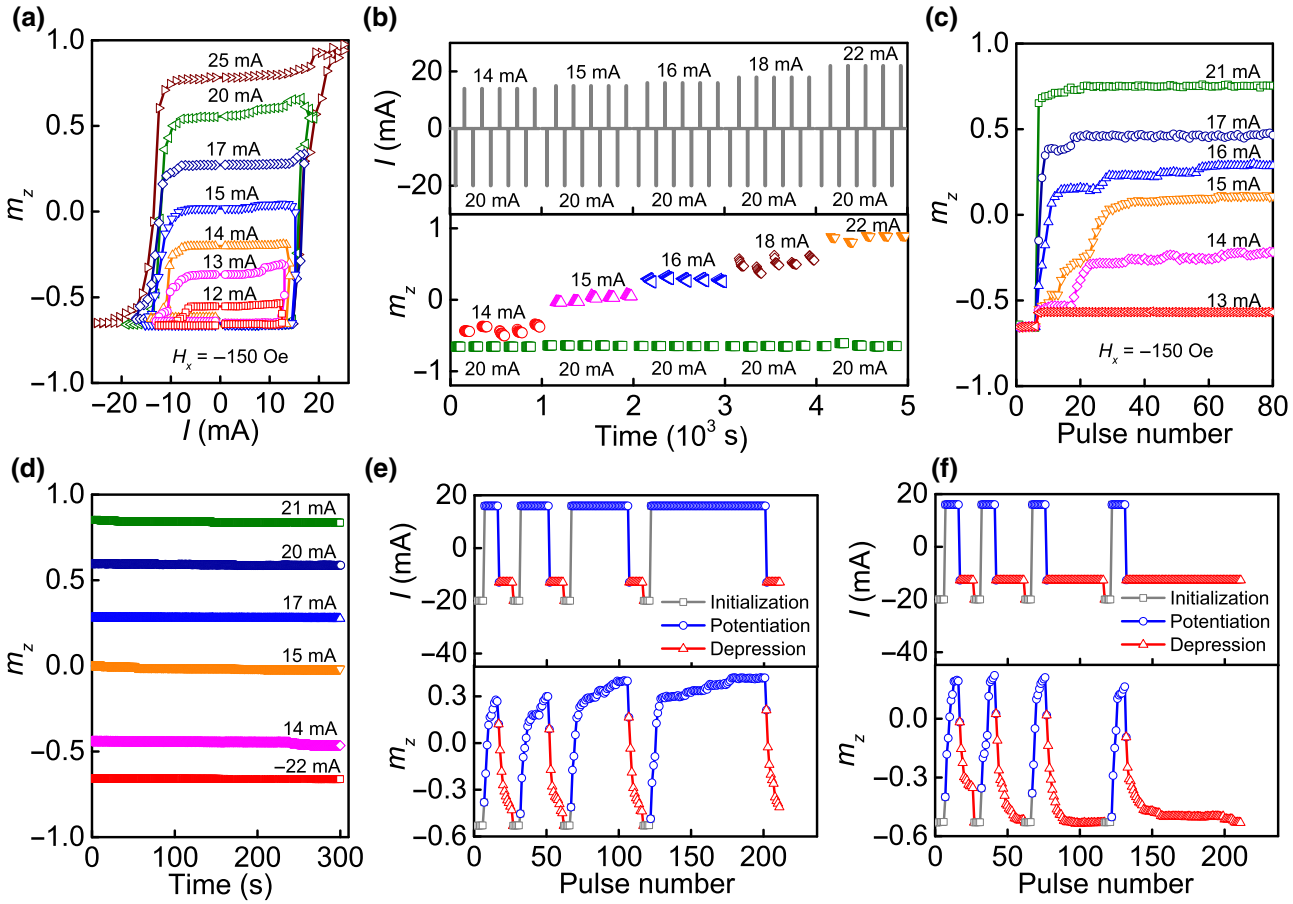

FIG. 4. (a) Current-induced magnetization-switching results for the (Co, Fe)B sample at $H_x = -150$ Oe with maximum writing current pulse amplitude in the range of 12–25 mA. (b) Repeated write-and-read measurements to set m_z into intermediate states by an individual writing pulse with an amplitude between 14–22 mA after an initialization pulse of −20 mA. (c) m_z as a function of the pulse number with fixed pulse magnitude between 13–22 mA. (d) The time decay curve of m_z after it is set into different intermediate states. (e) The applied current-pulse sequence and the m_z response to mimic long-term potentiation. (f) The applied current-pulse sequence and the m_z response to mimic long-term depression.

depicted in Fig. 4(b) (top panel). Basically, the intermediate states are set using an individual writing pulse between 14–22 mA after an initialization pulse of −20 mA. Meanwhile, the m_z state is always read by a 1-mA reading pulse. For each writing current amplitude, such a process is repeated for five times. As seen from the bottom panel of the figure, within the repeating period of a fixed writing amplitude, the intermediate states can be well reproduced. Besides the amplitude, different states of m_z can also be set by changing the repetition number of the current pulses. In this round of measurements, 80 writing pulses with fixed amplitude varying between 13–22 mA are applied after initialization by five pulses of −22 mA, and the m_z response is shown in Fig. 4(c). Indeed, at moderate magnitude of 14–17 mA, before reaching the stable state (after 40 pulses), m_z gradually increases with the increase of the pulse number. The increase of pulse number is in fact equivalent to the increase of the pulse width, which can increase the probability of domain-wall nucleation, depinning, and propagation processes, similar to the magnetic viscosity effect [53,55,56]. Furthermore, the robustness of the intermediate states is monitored by 1-mA reading current for a duration of 300 s after setting, and the results are shown in Fig. 4(c). It is clear that the decay of the signal within the monitored period is negligible. If we fit the curves with an exponential decay, a decay time on the order of 10^4–10^5 s could be estimated, which demonstrates the stability of these states. The observed behaviors in Figs 4(a)–4(d) are promising in neuromorphic computing since they can be used to imitate the behavior of synaptic devices, in particular, the long-term potentiation and depression (LTPD) effect [57]. To realize the effect in the sample, two more sets of the consecutive current pulse sequences are programmed as shown in Figs. 4(e) and 4(f) (top panel). As a start, m_z is always initialized by five pulses of −20 mA, and then followed by ten positive (negative) pulses with amplitude of 16 mA (−13 mA) and negative (positive) pulses with amplitude of −13 mA (16 mA) but varying repetition number of 10, 20, 40, and 80 in each repeating period. The responses of m_z to these pulse sequences are shown in Figs. 4(e) and 4(f) (bottom panel). As seen, the pulses with the same repetition number can reproducibly set the final m_z state; while m_z gradually increases (decreases) when the repetition number of positive (negative) pulses increases from 10 to 80. The increase (decrease) corresponds to the potentiation (depression) of a synapse. Similar behaviors can also be realized in the (Fe, Mn)Pt sample although its switching percentage is smaller than the (Co, Fe)B sample (results are not shown here). The results in Fig. 4 demonstrate the ability of the devices to imitate the LTPD effects in the supervised training process, in which synapse weight (m_z state here) can be tuned continuously and maintained for a long time (10^4–10^5 s). It is also worth pointing out that both the nonlinearity and asymmetry in the m_z response can be further eliminated through programing of nonidentical pulse pairs [57].

IV. CONCLUSIONS

In summary, we demonstrate current-induced magnetization switching in a FM1-Ti-FM2 trilayer structure in which the transversely polarized spin current generated by the easy-plane FM1 layer exerts a torque on the magnetization of the FM2 layer. The spin current is attributed to the combined effect of AHE and spin rotation at the top surface of the FM1 layer. The efficiency of spin-current generation in (Fe, Mn)Pt or (Co, Fe)B is characterized to be around 21% of that in Ta. Furthermore, the magnetization switching is found to exhibit multiple intermediate states, from which we realize LTPD effect as a synaptic device by programing the current pulse amplitude and number in sequences. This work together with our previous work shed some light on the spin-charge interconversion in FM materials with large SOC.

ACKNOWLEDGMENTS

The authors acknowledge the funding support by Singapore Ministry of Education, under its AcRF Tier 2 Grant (Grants No. MOE2017-T2-2-011 and No. MOE2018-T2-1-076).

[1] A. Chernyshov, M. Overby, X. Liu, J. K. Furdyna, Y. Lyanda-Geller, and L. P. Rokhinson, Evidence for reversible control of magnetization in a ferromagnetic material by means of spin–orbit magnetic field, Nat. Phys. **5**, 656 (2009).

[2] I. M. Miron, G. Gaudin, S. Auffret, B. Rodmacq, A. Schuhl, S. Pizzini, J. Vogel, and P. Gambardella, Current-driven spin torque induced by the Rashba effect in a ferromagnetic metal layer, Nat. Mater. **9**, 230 (2010).

[3] I. M. Miron, K. Garello, G. Gaudin, P. J. Zermatten, M. V. Costache, S. Auffret, S. Bandiera, B. Rodmacq, A. Schuhl, and P. Gambardella, Perpendicular switching of a single ferromagnetic layer induced by in-plane current injection, Nature **476**, 189 (2011).

[4] L. Liu, O. J. Lee, T. J. Gudmundsen, D. C. Ralph, and R. A. Buhrman, Current-Induced Switching of Perpendicularly Magnetized Magnetic Layers Using Spin Torque from the Spin Hall Effect, Phys. Rev. Lett. **109**, 096602 (2012).

[5] L. Liu, C. F. Pai, Y. Li, H. W. Tseng, D. C. Ralph, and R. A. Buhrman, Spin-torque switching with the giant spin Hall effect of tantalum, Science **336**, 555 (2012).

[6] T. Taniguchi, J. Grollier, and M. D. Stiles, Spin-Transfer Torques Generated by The Anomalous Hall Effect and Anisotropic Magnetoresistance, Phys. Rev. Appl. **3**, 044001 (2015).

[7] T. Taniguchi, Magnetoresistance generated from charge-spin conversion by anomalous Hall effect in metallic ferromagnetic/nonmagnetic bilayers, Phys. Rev. B **94**, 174440 (2016).

[8] S. S.-L. Zhang and S. Zhang, Angular dependence of anisotropic magnetoresistance in magnetic systems, J. Appl. Phys. **115**, 17C703 (2014).

[9] B. F. Miao, S. Y. Huang, D. Qu, and C. L. Chien, Inverse Spin Hall Effect in A Ferromagnetic Metal, Phys. Rev. Lett. **111**, 066602 (2013).

[10] D. Tian, Y. Li, D. Qu, S. Y. Huang, X. Jin, and C. L. Chien, Manipulation of pure spin current in ferromagnetic metals independent of magnetization, Phys. Rev. B **94**, 020403(R) (2016).

[11] H. Wu, C. H. Wan, Z. H. Yuan, X. Zhang, J. Jiang, Q. T. Zhang, Z. C. Wen, and X. F. Han, Observation of pure inverse spin Hall effect in ferromagnetic metals via ferromagnetic/antiferromagnetic exchange-bias structures, Phys. Rev. B **92**, 054404 (2015).

[12] C. Qin, S. Chen, Y. Cai, F. Kandaz, and Y. Ji, Nonlocal electrical detection of spin accumulation generated by anomalous Hall effect in mesoscopic $Ni_{81}Fe_{19}$ films, Phys. Rev. B **96**, 134418 (2017).

[13] K. S. Das, J. Liu, B. J. van Wees, and I. J. Vera-Marun, Efficient injection and detection of out-of-plane spins via the anomalous spin Hall effect in permalloy nanowires, Nano Lett. **18**, 5633 (2018).

[14] K. S. Das, W. Y. Schoemaker, B. J. van Wees, and I. J. Vera-Marun, Spin injection and detection via the anomalous spin Hall effect of a ferromagnetic metal, Phys. Rev. B **96**, 220408(R) (2017).

[15] J. Cramer, A. Ross, S. Jaiswal, L. Baldrati, R. Lebrun, and M. Kläui, Orientation-dependent direct and inverse spin Hall effects in $Co_{60}Fe_{20}B_{20}$, Phys. Rev. B **99**, 104414 (2019).

[16] A. Bose, D. D. Lam, S. Bhuktare, S. Dutta, H. Singh, Y. Jibiki, M. Goto, S. Miwa, and A. A. Tulapurkar, Observation of Anomalous Spin Torque Generated by A Ferromagnet, Phys. Rev. Appl. **9**, 064026 (2018).

[17] J. D. Gibbons, D. MacNeill, R. A. Buhrman, and D. C. Ralph, Reorientable Spin Direction for Spin Current Produced by The Anomalous Hall Effect, Phys. Rev. Appl. **9**, 064033 (2018).

[18] S. Iihama, T. Taniguchi, K. Yakushiji, A. Fukushima, Y. Shiota, S. Tsunegi, R. Hiramatsu, S. Yuasa, Y. Suzuki, and H. Kubota, Spin-transfer torque induced by the spin anomalous Hall effect, Nat. Electron. **1**, 120 (2018).

[19] Y. Yang, Z. Luo, H. Wu, Y. Xu, R. W. Li, S. J. Pennycook, S. Zhang, and Y. Wu, Anomalous Hall magnetoresistance in a ferromagnet, Nat. Commun. **9**, 2255 (2018).

[20] S. C. Baek, V. P. Amin, Y. W. Oh, G. Go, S. J. Lee, G. H. Lee, K. J. Kim, M. D. Stiles, B. G. Park, and K. J. Lee, Spin currents and spin-orbit torques in ferromagnetic trilayers, Nat. Mater. **17**, 509 (2018).

[21] A. M. Humphries, T. Wang, E. R. J. Edwards, S. R. Allen, J. M. Shaw, H. T. Nembach, J. Q. Xiao, T. J. Silva, and X. Fan, Observation of spin-orbit effects with spin rotation symmetry, Nat. Commun. **8**, 911 (2017).

[22] S. Emori, T. Nan, A. M. Belkessam, X. Wang, A. D. Matyushov, C. J. Babroski, Y. Gao, H. Lin, and N. X. Sun, Interfacial spin-orbit torque without bulk spin-orbit coupling, Phys. Rev. B **93**, 180402(R) (2016).

[23] W. Wang, T. Wang, V. P. Amin, Y. Wang, A. Radhakrishnan, A. Davidson, S. R. Allen, T. J. Silva, H. Ohldag, D. Balzar, B. L. Zink, P. M. Haney, J. Q. Xiao, D. G. Cahill, V. O. Lorenz, and X. Fan, Anomalous spin-orbit torques in magnetic single-layer films, Nat. Nanotechnol. **14**, 819 (2019).

[24] V. P. Amin, J. Zemen, and M. D. Stiles, Interface-Generated Spin Currents, Phys. Rev. Lett. **121**, 136805 (2018).

[25] V. P. Amin, J. Li, M. D. Stiles, and P. M. Haney, Intrinsic spin currents in ferromagnets, Phys. Rev. B **99**, 220405(R) (2019).

[26] G. Qu, K. Nakamura, and M. Hayashi. Magnetization direction dependent spin Hall effect in 3d ferromagnets. arXiv:1901.10740.

[27] C. O. Pauyac, M. Chshiev, A. Manchon, and S. A. Nikolaev, Spin Hall and Spin Swapping Torques in Diffusive Ferromagnets, Phys. Rev. Lett. **120**, 176802 (2018).

[28] T. Seki, S. Iihama, T. Taniguchi, and K. Takanashi. Large spin anomalous Hall effect in L10–FePt: Symmetry and magnetization switching, Phys. Rev. B **100**, 144427 (2019).

[29] L. Liu, J. Yu, R. González-Hernández, J. Deng, W. Lin, C. Li, C. Zhou, T. Zhou, H. Y. Yoong, Q. Qin, H. Wang, X. Han, B. Dupé, J. Sinova, and J. Chen. Electrical switching of perpendicular magnetization in L10 FePt single layer. arXiv:1807.08244.

[30] H. Wu, S. A. Razavi, Q. Shao, X. Li, K. L. Wong, Y. Liu, G. Yin, and K. L. Wang, Spin-orbit torque from a ferromagnetic metal, Phys. Rev. B **99**, 184403 (2019).

[31] M. Haidar, A. A. Awad, M. Dvornik, R. Khymyn, A. Houshang, and J. Akerman, A single layer spin-orbit torque nano-oscillator, Nat. Commun. **10**, 2362 (2019).

[32] C. Safranski, E. A. Montoya, and I. N. Krivorotov, Spin-orbit torque driven by a planar Hall current, Nat. Nanotechnol. **14**, 27 (2019).

[33] Z. Luo, Q. Zhang, Y. Xu, Y. Yang, X. Zhang, and Y. Wu, Spin-Orbit Torque in A Single Ferromagnetic Layer Induced by Surface Spin Rotation, Phys. Rev. Appl. **11**, 064021 (2019).

[34] V. P. Amin and M. D. Stiles, Spin transport at interfaces with spin-orbit coupling: Formalism, Phys. Rev. B **94**, 104419 (2016).

[35] V. P. Amin and M. D. Stiles, Spin transport at interfaces with spin-orbit coupling: Phenomenology, Phys. Rev. B **94**, 104420 (2016).

[36] J. Kessler, *Polarized Electrons* (Springer Science & Business Media, Berlin, Heidelberg, 2013), pp. 57.

[37] J. C. Slonczewski, Current-driven excitation of magnetic multilayers, J. Magn. Magn. Mater. **159**, L1 (1996).

[38] L. Berger, Emission of spin waves by a magnetic multilayer traversed by a current, Phys. Rev. B **54**, 9353 (1996).

[39] M. D. Stiles and A. Zangwill, Anatomy of spin-transfer torque, Phys. Rev. B **66**, 014407 (2002).

[40] J. C. Slonczewski, Conductance and exchange coupling of two ferromagnets separated by a tunneling barrier, Phys. Rev. B **39**, 6995 (1989).

[41] C. O. Avci, K. Garello, C. Nistor, S. Godey, B. Ballesteros, A. Mugarza, A. Barla, M. Valvidares, E. Pellegrin, A. Ghosh, I. M. Miron, O. Boulle, S. Auffret, G. Gaudin, and P. Gambardella, Fieldlike and antidamping spin-orbit torques in as-grown and annealed Ta/CoFeB/MgO layers, Phys. Rev. B **89**, 214419 (2014).

[42] K. Garello, I. M. Miron, C. O. Avci, F. Freimuth, Y. Mokrousov, S. Blugel, S. Auffret, O. Boulle, G. Gaudin, and P. Gambardella, Symmetry and magnitude of spin-orbit torques in ferromagnetic heterostructures, Nat. Nanotechnol. **8**, 587 (2013).

[43] X. Qiu, K. Narayanapillai, Y. Wu, P. Deorani, D. H. Yang, W. S. Noh, J. H. Park, K. J. Lee, H. W. Lee, and H. Yang, Spin-orbit-torque engineering via oxygen manipulation, Nat. Nanotechnol. **10**, 333 (2015).

[44] S. Yang, J. Lee, G. An, J. Kim, W. Chung, and J. Hong, Ta thickness-dependent perpendicular magnetic anisotropy features in Ta/CoFeB/MgO/W free layer stacks, Thin Solid Films **587**, 39 (2015).

[45] M. Li, J. Lu, M. Akyol, X. Chen, H. Shi, G. Han, T. Shi, G. Yu, A. Ekicibil, N. Kioussis, P. V. Ong, P. K. Amiri, and K. L. Wang, The impact of hf layer thickness on the perpendicular magnetic anisotropy in Hf/CoFeB/MgO/Ta films, J. Alloys Compd. **694**, 76 (2017).

[46] Y. W. Oh, K. D. Lee, J. R. Jeong, and B. G. Park, Interfacial perpendicular magnetic anisotropy in CoFeB/MgO structure with various underlayers, J. Appl. Phys. **115**, 17C724 (2014).

[47] V. Sokalski, M. T. Moneck, E. Yang, and J. G. Zhu, Optimization of Ta Thickness for Perpendicular Magnetic Tunnel Junction Applications in the MgO-FeCoB-Ta System, Appl. Phys. Lett. **101**, 072411 (2012).

[48] C. F. Pai, M. Mann, A. J. Tan, and G. S. D. Beach, Determination of spin torque efficiencies in heterostructures with perpendicular magnetic anisotropy, Phys. Rev. B **93**, 144409 (2016).

[49] J. Han, A. Richardella, S. A. Siddiqui, J. Finley, N. Samarth, and L. Liu, Room-Temperature Spin-Orbit Torque Switching Induced by a Topological Insulator, Phys. Rev. Lett. **119**, 077702 (2017).

[50] A. Thiaville, S. Rohart, É Jué, V. Cros, and A. Fert, Dynamics of Dzyaloshinskii domain walls in ultrathin magnetic films, Europhys. Lett. **100**, 57002 (2012).

[51] L. Zhu, D. C. Ralph, and R. A. Buhrman, Spin-Orbit Torques in Heavy-Metal-Ferromagnet Bilayers with Varying Strengths of Interfacial Spin-Orbit Coupling, Phys. Rev. Lett. **122**, 077201 (2019).

[52] O. J. Lee, L. Liu, C. F. Pai, Y. Li, H. W. Tseng, P. G. Gowtham, J. P. Park, D. C. Ralph, and R. A. Buhrman, Central role of domain wall depinning for perpendicular magnetization switching driven by spin torque from the spin Hall effect, Phys. Rev. B **89**, 024418 (2014).

[53] K. S. Lee, S. W. Lee, B. C. Min, and K. J. Lee, Thermally activated switching of perpendicular magnet by spin-orbit spin torque, Appl. Phys. Lett. **104**, 072413 (2014).

[54] K. J. Kim, J. Ryu, G. H. Gim, J. C. Lee, K. H. Shin, H. W. Lee, and S. B. Choe, Electric Current Effect on The Energy Barrier of Magnetic Domain Wall Depinning: Origin of the Quadratic Contribution, Phys. Rev. Lett. **107**, 217205 (2011).

[55] A. Kurenkov, S. DuttaGupta, C. Zhang, S. Fukami, Y. Horio, and H. Ohno, Artificial neuron and synapse realized in an antiferromagnet/ferromagnet heterostructure using dynamics of spin-orbit torque switching, Adv. Mater. **31**, e1900636 (2019).

[56] S. Okamoto, N. Kikuchi, O. Kitakami, and Y. Shimada, Magnetization reversal process in FePt L10 nanoparticles, Scr. Mater. **53**, 395 (2005).

[57] S. Yu, Neuro-inspired computing with emerging nonvolatile memory, Proc. IEEE **106**, 260 (2018).